

MODELING THE EFFECT OF WATER DEPTH ON ROCK CUTTING PROCESSES WITH THE USE OF DISCRETE ELEMENT METHOD

R.L.J. Helmons¹, S.A. Miedema² and C. van Rhee³

Abstract: Whether it is for the construction of ports on new locations, the widening of canals through mountainous terrain or deep sea mining, efficient rock cutting is still one of the challenges that the dredging industry is facing. This gets more challenging by the fact that in dredging rock cutting is most of the time an underwater process. The water that is surrounding the rock and in the pores of the rock can have a major influence on the rock cutting process by increasing the required cutting forces.

During cutting, the rock matrix deforms and as a result local fluid pressure differences will occur. The magnitude of these pressure differences, and thus its effect on the cutting process, depends on the water depth and the cutting velocity. As a result of this, rock that is brittle under atmospheric conditions will behave more ductile in larger water depths. This paper focuses on the effect that the water depth can have on the cutting process.

The Discrete Element Method (DEM) has been successful in the modeling of rock cutting processes for dry, land-based operations. In order to make the DEM useful for underwater excavations, it has been extended with a fluid coupling. Results of this extension with respect to the effect of water depth will be presented. A clear distinction between shallow water (brittle) and deep water cutting (ductile) is observed. The newly developed method will give more insight in the physical processes that occur during cutting and it can help to improve the design and operational guidelines of the cutting equipment and processes.

Key words: rock mechanics, rock cutting

¹ Delft University of Technology, Netherlands, r.l.j.helmons@tudelft.nl

² Delft University of Technology, Netherlands, s.a.miedema@tudelft.nl

³ Delft University of Technology, Netherlands, c.vanrhee@tudelft.nl

1 INTRODUCTION

A variety of rock cutting works are carried out in dredging engineering by means of different machines and cutting tools. Whether it is for the construction of ports on new locations, the widening of canals through mountainous terrain or deep sea mining, efficient rock cutting is still one of the challenges that the dredging industry is facing. The rock cutting process for dredging purposes is even more complex compared to dry, land-based excavations due to the fact that in dredging the rock is most often cut under water. The water that is present both in and surrounding the rock and in the pores of the rock can have a major influence on the rock cutting process by increasing the required cutting forces. Therefore, this paper focuses on the effects that arise due to the presence of a fluid (seawater) on the rock cutting process, especially the effect of the fluid pressure in the pores of the rock and surrounding the rock.

The basic physical phenomena that occur during rock cutting are fracturing and fragmentation of the rock due to a mechanical action of the cutting tool. The rock failure mechanism during cutting depends on many factors, most important being the type of rock and rock properties, tool geometry and its position with respect to the rock. Depending on the type of rock, rock properties and the conditions the rock is in, a distinction can be made between brittle and ductile failure. Rock chips are formed and separated due to the combined action of shear and tensile fracture, which is initiated in a crushed zone (cataclasis) near the tool tip and transmitted into the intact rock, see figure 1.

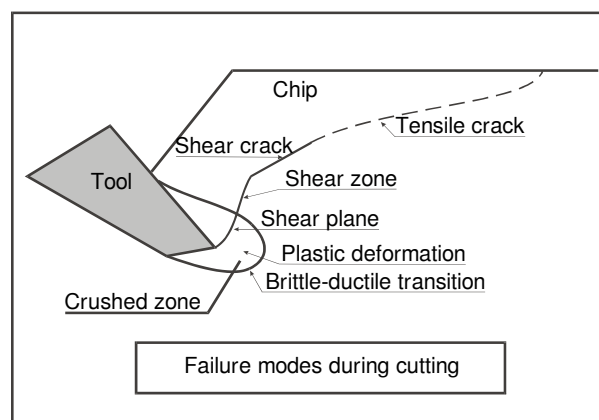


Figure 1. Phenomenological model of rock cutting process, based on van Kesteren (1995)

Optimization of the rock cutting equipment requires knowledge about the cutting process, which can be obtained not only from experiments and field measurements, but also by simulations. The cutting process is influenced by four different groups of factors:

- Properties of rock and rock mass
- Design of the cutting tool
- Operational parameters such as cutting depth, cutting speed, line spacing, etc.
- Environmental parameters such as dry, submerged, water depth, etc.

All these factors influence the performance and efficiency of the cutting process.

Different models have been used to predict cutting force for given cutting tool and rock properties. These models are based on experimental, analytical and numerical approaches. Experimental studies of rock cutting enabled better understanding of rock-tool interaction and provided information necessary for theoretical modeling. Simple analytical models have been created in attempt to describe the cutting processes. One of the earliest models is a 2D model developed by Evans (1965) for rock cutting with drag picks. In this model it is assumed that the breakage mechanism is essentially tensile and occurs along the failure surface, which approximates a circular arc. Another 2D model has been developed by Nishimatsu (1972) who assumed that failure is purely due to shear and occurs along a plane. Miedema (2014) adapted the Nishimatsu model, such that it is able to deal with tensile and shear failures. Although these rock cutting models are quite effective to predict the cutting forces, they are limited in their level of detail on the rock cutting process.

The rock failure process during cutting can be traced in more detail by using appropriate numerical models. A number of numerical studies of rock cutting use the finite element method (FEM). However, the FEM is based on continuum mechanics theory of material modeling. Because of that, the FEM has serious issues in representing the discontinuities that occur during cutting. Special formulations are necessary to introduce the possibility of dis-continuum analysis of rock fracture. In many cases, analysis of rock cutting by the finite element method is limited to the initial stage of major chip formation since the formulation used does not allow for the continuation

of the analysis in the post-failure stage in which the process goes through the transition of rock mechanics to granular flow.

The discrete element method (DEM) can take into account most kinds of discontinuities and material failure characterized with multiple fractures, which makes it a suitable tool to study rock cutting. The discrete element was successfully applied to simulation of rock cutting by Huang (1999); Huang et al. (2013) and Rojek et al. (2011). A 3D DEM model of rock cutting with conical picks was developed by Su and Akcin (2011). Several attempts have been done to model the rock cutting process for (oil/gas) drilling. For instance, the model of Huang was used by Lei and Kaitkay (2003) to study rock cutting under a high confining pressure. Mendoza Rizo (2013) used another formulation to define the effect of a hydrostatic pressure and compared his results with those of Lei and Kaitkay. Although the approaches of Lei and Kaitkay (2003) and Mendoza Rizo (2013) are able to mimic the rock cutting process under a high pressure, they both neglected the effects of pore pressures and fluid velocity (hydraulic conductivity).

2 CONFINING AND EFFECTIVE STRESS

The flow of fluid in and surrounding a rock is the main phenomenon that controls the effective stress in a rock. These mechanisms have long been recognized to cause the difference in strain-rate dependency of the rock strength for dry and saturated rock samples. Pore pressures work as a counteracting effect on the normal stress within a rock, which is expressed by Terzaghi's law of effective stress (Terzaghi (1943)):

$$\sigma = \sigma' + p \quad (1)$$

with total stress σ , effective stress σ' and pore pressure p . However, this generalization of Terzaghi's law is only applicable in quasi-static processes, where the local variations in pore pressure are negligible. This can be estimated with the pore Peclet number, which can be interpreted as the ratio of deformation rate over the pore pressure dissipation rate. In case of rock cutting, different definitions of the pore Peclet number exist. According to Detournay and Atkinson (2000), the pore Peclet number ξ_{Pe} is given by

$$\xi_{Pe} = \frac{v_c t_c}{4D} = \frac{v_c t_c n \mu C_f}{4\kappa} \quad (2)$$

with cutting velocity v_c , cutting thickness t_c , pore pressure diffusivity coefficient D , dynamic fluid viscosity μ , porosity n , fluid compressibility C_f and intrinsic permeability κ , in m^2 . According to Detournay and Atkinson (2000), three different regimes can be distinguished

- Low speed regime ($0 < \xi_{Pe} < 0.001$): the rock responds in a drained manner during failure and $\Delta p \simeq 0$.
- Transient regime ($0.001 < \xi_{Pe} < 10$): pore pressure and rock deformation are weakly coupled.
- High speed regime ($\xi_{Pe} > 10$): pore pressure and rock deformation are strongly coupled, during failure the rock responds in an undrained manner.

Detournay and Atkinson (2000) based their definitions on the application of drilling (small cutting thicknesses, in the order of mm's or smaller). A somewhat similar definition is used by van Kesteren (1995) for dredging purposes (large cutting thicknesses, in the order of several to tens of cm's). Except in these definitions, the regimes are divided in $\xi_{Pe} < 1$, $1 < \xi_{Pe} < 10$ and $10 < \xi_{Pe}$. The difference between the defined drained and transitional regimes is most likely due to differences in their applications, being a large difference in hydrostatic pressures (in the order of several bars for dredging applications and up to tens of MPa's for drilling applications).

When cutting saturated rock, dilative and compactive effects occur simultaneously, which makes it difficult to distinguish these effects and their influences during cutting. In uni-axial and tri-axial tests these effects are easier to distinguish. The most profound phenomena that occur in the transient and high speed regime are:

- Compactive weakening (Swan et al. (1989))
- Dilative strengthening (often erroneously referred to as dilation hardening) (Brace and Martin III (1968), Swan et al. (1989))

Compactive weakening is related to the compression of the pore bodies in the rock. When these are being compressed, their volume decreases, resulting in an increase in pore pressure. This increase results in a larger pressure gradient through the rock, which 'helps' in the deformation of the rock as an additional load, see figure 2 for a schematic overview. The compactive weakening effect is also noted in single cutter tests of Zijssling (1987) on Pierre shale.

During dilation due to the creation of new and the extension of existing microcracks, the porosity of the rock increases and the pore pressure of an effectively undrained sample locally drops. This results in an increase of the effective stress and thus an increase in apparent strength. A schematic overview of dilatancy strengthening is shown in figure 3.

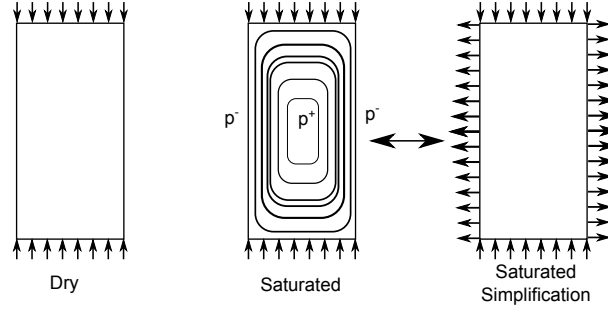


Figure 2. Schematic overview of compactive weakening

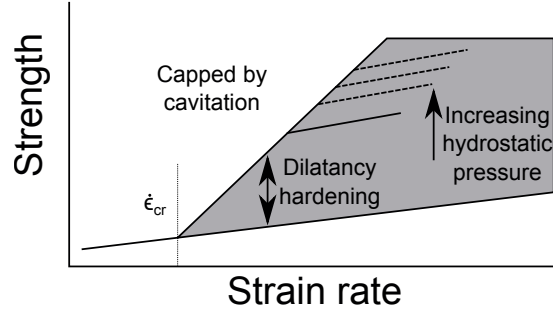


Figure 3. Dilative strengthening, based on Brace and Martin III (1968)

Below a critical strain rate $\dot{\epsilon}_{cr}$, there is no significant effect of the pore fluid on the failure of the rock. At strain rates above $\dot{\epsilon}_{cr}$, the apparent strength of a rock increases more compared to that of a drained or dry sample. However, the strengthening effect is limited by cavitation.

In case of cavitation, the pressure in the dilative zone drops below the vapour pressure of the fluid, causing the pore fluid to evaporate. As a result the pressure in the pores can hardly drop and the bulk compressibility of the fluid increases several orders of magnitude. As a result, Δp is limited. The maximum achievable Δp , and thus the maximum dilative strengthening, increases linearly with the hydrostatic pressure.

3 METHOD

3.1 Rock

In DEM, the solid material is represented as a collection of particles (these can be any arbitrarily shape, most often spheres in 3D or discs with unit thickness in 2D are used for the sake of simplicity) that have mutual interactions in normal and tangential directions. This paper gives the description and results in 2D. The translational and rotational motion of a particle is governed by the standard equations of rigid body mechanics

$$m_i \vec{a}_i = \vec{F}_i \quad (3)$$

$$I_i \vec{\alpha}_i = \vec{T}_i \quad (4)$$

\vec{F} and \vec{T} are the sums of all forces and moments applied to the particle i due to external loading, contact interactions with neighboring objects and from damping in the system. Due to the high computational effort that is needed to calculate the forces acting on the particles, the equations of are integrated with an explicit multi-step time integration scheme, i.e. the velocity Verlet scheme.

$$\vec{r}_i^{n+1} = \vec{r}_i^n + \vec{v}_i^n \Delta t + \frac{1}{2} \vec{a}_i^n \Delta t^2 \quad (5)$$

$$\vec{v}_i^{n+1/2} = \vec{v}_i^n + \frac{1}{2} \vec{a}_i^n \Delta t \quad (6)$$

$$\vec{a}_i^{n+1} = \frac{1}{m_i} \sum \vec{F}_i^{n+1} \quad (7)$$

$$\vec{v}_i^{n+1} = \vec{v}_i^{i+1/2} + \frac{1}{2} \vec{a}_i^{n+1} \Delta t \quad (8)$$

It needs mentioning that \vec{F}^{n+1} is actually a function of \vec{r}^{n+1} and $\vec{v}^{n+1/2}$. Because of the use of an explicit scheme, there is a limitation on the size of the timestep to ensure a stable solution, meaning $\Delta t \leq \Delta t_{cr}$. Δt_{cr} is approximated by the highest of natural frequencies of a contact pair.

The interaction force between a pair of particles can either consist of a collision type or a bond type of interaction. In both cases the force is composed of normal and tangential components, with

$$\vec{F} = \vec{F}_n + \vec{F}_t = \vec{n}F_n + \vec{t}F_t \quad (9)$$

where \vec{n} is the unit vector normal to the particle surface at the point of interaction. The contact forces F_n and F_t are determined with a constitutive model for the interaction. At the beginning of each simulation, a bond is installed between neighboring particles. These bonds are defined by a linear elastic perfect brittle model (see figure 4), meaning that a bond breaks immediately when its strength is exceeded. Note that a bond can break either in normal (tension) or in tangential (shear) direction and not in compressive direction (macroscopic compressive failure is considered as a localization of many micro-shear and tensile failures). After a bond is broken, the bond will be removed from the simulation. Besides bonds, there are also collisional interactions. In these interactions the normal force is only active in compressive direction and the tangential force can be either static or dynamic friction.

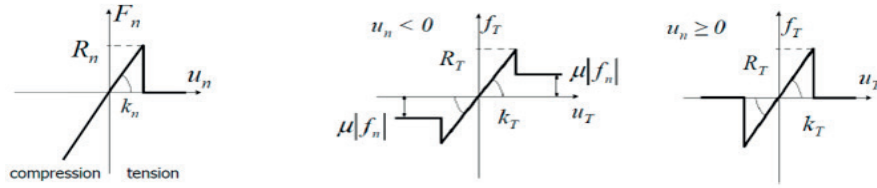


Figure 4. Linear elastic perfect brittle bond model: (left) normal direction, (middle) shear direction with contact after failure and (right) shear direction without contact after failure

To reach a quasi-static equilibrium, it is necessary that the kinetic energy dissipates. Especially since the DEM is a highly dynamics approach, damping is required. This is done by application of numerical damping, as in Potyondy and Cundall (2004) and is often used in DEM-applications for rock. The damping force is in the form of

$$\vec{F}_d = -\alpha_d \left| \sum \vec{F} \right| \text{sign}(\vec{v}) \quad (10)$$

with damping coefficient α_d .

The DEM can be regarded as a micromechanical model, with the contact and bond model parameters being microparameters. It is assumed that with the adequate micromechanical parameters macroscopic rock properties are obtained, of which the Young's modulus E , Poisson ratio ν , and compressive and tensile strengths σ_c and σ_t are the most relevant. These properties will be used in calibrating the micromechanical model to sufficiently mimic the macroscopic rock mechanics.

3.2 Fluid pressure

The effect of a rapidly changing effective stress is modeled with the use of a pore pressure diffusion equation, as in Coussy (2004). This equation is based on the combination of mass conservation, Darcy flow and a constitutive equation for the compressibility of the pore fluid, given respectively by

$$\frac{D\zeta}{Dt} + \nabla \cdot \vec{u} = 0 \quad (11)$$

$$\vec{u} = -\frac{\kappa}{\mu} \nabla p \quad (12)$$

$$p = M (\zeta - \alpha \epsilon_v) \quad (13)$$

which through substitution results in the pore pressure diffusion equation given by

$$\frac{Dp}{Dt} - M \nabla \cdot \left(\frac{\kappa}{\mu} \nabla p \right) = -\alpha M \frac{D\epsilon_v}{Dt} \quad (14)$$

with pressure p , fluid bulk modulus M , intrinsic permeability κ , dynamic fluid viscosity μ , effective stress coefficient α and volumetric strain ϵ_v .

The coupling of the discrete data obtained from the DEM computations with the pore pressure diffusion equation (3.2) is obtained by using a Smoothed Particle (SP) approach. SP is a kernel interpolation technique that is

originally developed by Lucy (1977). DEM and SP work in a co-located fashion, meaning that both methods use the same discretisation points.

In the DEM-SP model, the discretized particles are taken from a particle size distribution and randomly stacked together. The unstructured positions and random size (and thus mass) of the particles can easily result in numerical instabilities and inaccuracies. To adjust for the random size and positioning of the particles, the Corrective Smoothed Particle Approach (CSPM) is used (Chen et al. (1999)).

In CSPM, the kernel interpolation of a field quantity A (which can be any arbitrary parameter) is calculated by

$$A(\vec{r}_i) = \frac{\sum_j A_j m_j W(\vec{r}_i - \vec{r}_j, h)}{\sum_j m_j W(\vec{r}_i - \vec{r}_j, h)} \quad (15)$$

with particle mass m , kernel function W , position r , smoothing length h , index i for particle under consideration and index j for neighboring particles (including particle i). In a similar fashion, the first order derivative of a function A is determined by

$$\nabla_i A(\vec{r}_i) = \frac{\sum_j (A_i - A_j) m_j \nabla W(\vec{r}_i - \vec{r}_j, h)}{\sum_j (\vec{r}_i - \vec{r}_j) m_j \nabla W(\vec{r}_i - \vec{r}_j, h)} \quad (16)$$

where ∇_i is the gradient with respect to particle i . Higher order derivatives cannot be calculated directly. The first derivative is necessary to determine the volumetric strain rate in equation (3.2),

$$\dot{\epsilon}_v = \nabla \cdot \vec{v} = \frac{\partial v_x}{\partial x} + \frac{\partial v_y}{\partial y} \quad (17)$$

Here the Wendland C2 kernel function is used Wendland (1995)

$$W = \begin{cases} \frac{7}{\pi^2} (1 - R)^4 (4R + 1) & \text{if } R \leq 1 \\ 0 & \text{if } R > 1 \end{cases} \quad (18)$$

where

$$R = \frac{\|\vec{r}_i - \vec{r}_j\|}{h} \quad (19)$$

To calculate the diffusive term in (3.2), we make use of the results of Cleary and Monaghan (1999):

$$\nabla \cdot \kappa \nabla p = \sum_j \frac{m_j (\kappa_i + \kappa_j)}{\rho_i} (p_i - p_j) \frac{\vec{n}_{ij} \cdot \nabla W(\vec{r}_i - \vec{r}_j, h)}{\|\vec{r}_i - \vec{r}_j\|} \quad (20)$$

where \vec{n}_{ij} is the normal unit vector of the neighboring particle centers. Note that here κ is a property of the particles and thus that it can differ throughout the rock sample. In our case, it is assumed that κ is constant.

Two way coupling is applied every timestep. DEM is advanced half a timestep, based on the intermediate velocities the volumetric strain rate is calculated with SP. This is then used to advance the pore pressure diffusion one timestep in a forward Euler scheme. The local pressure gradient of the fluid is calculated based on the new pore pressure distribution. The pressure gradient is then added as an interaction force to the sum of forces acting on the particles through

$$\vec{F} = -\nabla p \frac{\pi d_p^2 w}{4} \quad (21)$$

with particle diameter d_p and unit thickness w . Finally the DEM is advanced the second half timestep. See figure 5 for the flowchart of this coupling scheme.

It is possible that the fluid pressure drops below the vapour pressure during simulations. When this happens, the liquid will vaporize. As a result, the compressibility of the fluid of increases with several orders of magnitude. In the simulations, this is modeled through a simplified approach. When the pressure drops below the pressure minimum, the pressure value is fixed at the minimum pressure. From thereon it is only possible to increase the pressure by having fluid flow towards the cavitated zone, so if

$$p_i < p_{min} \quad \text{then} \quad p_i = p_{min} \quad \text{and} \quad \frac{\partial p_i}{\partial t} = \max\left(\frac{\partial p_i}{\partial t}, 0\right) \quad (22)$$

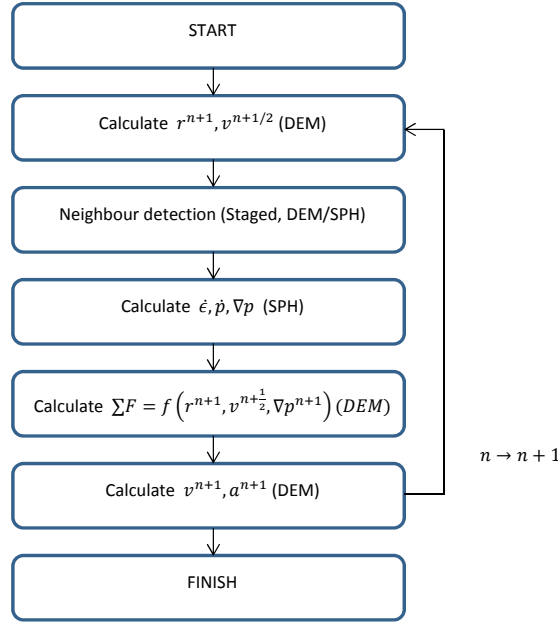


Figure 5. Flowchart of the DEM-SP method

3.3 Boundary conditions

In DEM-SP, boundary conditions have to be applied for both the rock and fluid phase. For rock this is done by restricting or prescribing the motion of specific particles or walls. In case of the fluid pressure, the boundary conditions are somewhat harder to set. The SP discretisation of (3.2) in itself automatically applies Neumann boundary condition (zero gradient), meaning that it allows no fluid flow across the boundaries of the rock. This is applicable in the case where equipment is moving through the rock (cutting teeth, compressive tests, splitting tests, etc.). In case of a rock boundary that is in contact with clear fluid, like the top layer of the seabed, a Dirichlet boundary condition (fixed value, such as hydrostatic pressure) is applied. However, the boundaries of the rock may change during the simulation. Therefore it is necessary to use a method to determine what particles are part of the rock boundary. To determine this, we make use of the divergence of position, as suggested by Muhammad et al. (2013).

$$\nabla \cdot \vec{r} = \frac{\partial x}{\partial x} + \frac{\partial y}{\partial y} = 2 \quad (23)$$

This is applied to the standard Smoothed Particle approach of Lucy (1977), because otherwise the CSPM in equation (3.2) automatically corrects for the particle deficiency, always setting at a value of 2.

$$\nabla_i A(\vec{r}_i) = \sum_j m_j \frac{A_j}{\rho_j} \nabla W(\vec{r}_i - \vec{r}_j, h) \quad (24)$$

In the interior domain of the rock, equation (3.3) is valid. However, at the boundaries this value differs due to particle deficiency, see figure 6. Here, particles with $\nabla \cdot \vec{r} \leq 1.5$ are considered to be part of the boundary. With this technique, the particles that require a Dirichlet boundary condition can now be identified.

4 RESULTS

The input and output parameters of the simulated rock are shown in table 1. For this paper, the parameters were chosen to represent a weak sandstone with a relatively high permeability.

A set of cutting simulations has been performed with varying water depth. Simulations have run at depths of 0, 10, 40, 100, 250, 1000 and 2000 meters. All other parameters have been kept constant. The larger water depths are simulated to investigate what differences there might be between dredging (< 30 m) and deep sea mining applications. In these simulations, rock is cut with a chisel at a 60 deg angle, a cutting depth of 0.02 meter, a cutting velocity of 1 m/s. Furthermore, it is assumed that the pore pressure is initially equal to the hydrostatic pressure. These conditions are chosen to cover both dredging and deep sea mining applications. Although the cutting velocity and the cutting depth are smaller than often used for dredging purposes, here it is chosen to do it at lower values for academic purposes.

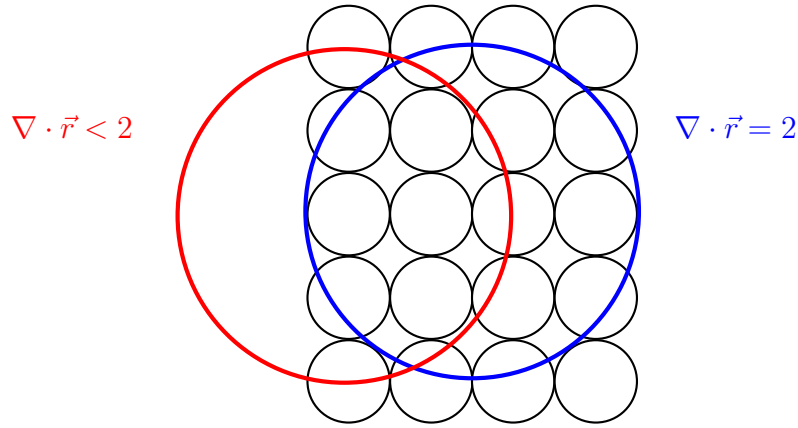


Figure 6. Schematic overview of particle deficiency

Table 1. Input and output parameters of simulated rock

Model input		Model output		Geometry	
K_n	10 GPa	UCS	13.8 MPa	Block height	0.1 m
K_s	25 GPa	BTS	2.55 MPa	Block width	0.2 m
T_n	10 kNm ⁻¹	E	5.5 GPa	Cutting depth	0.02 m
T_s	20 kNm ⁻¹	ν	0.22	Tool angle	60 deg
μ_{grain}	1			Tool width	0.02 m
R	0.0002 – 0.0004 mm			Water depth	0 – 2000 m
α	0.5			Cutting velocity	1 m/s
κ	$1 \cdot 10^{-14} \text{m}^2$				
n	0.18				
ρ_{grain}	2800 kgm ⁻³				
h	0.0015 m				
M	2 GPa				
μ_{fluid}	0.001 Pas				

The resulting averaged cutting forces are shown in figure 8. Note that the vertical force is directed such that the tool has to be pushed into the rock (downwards). In some areas, the average pore pressure is calculated, the locations of these areas are shown in figure 7 and move along with the movement of the chisel. The averaged results of these pressure measurements are shown in figures 9 and 10, here referred to as P_1 , P_2 and P_3 . All nodes cover the same size, an area of 2.5 mm in width and height. Node 1 is located exactly at the tool tip, node 2 is 12.5 mm in front and 10 mm above the tool tip and node 3 is 30 mm in front of the tool tip. The position of the nodes is kept the same for all simulations.

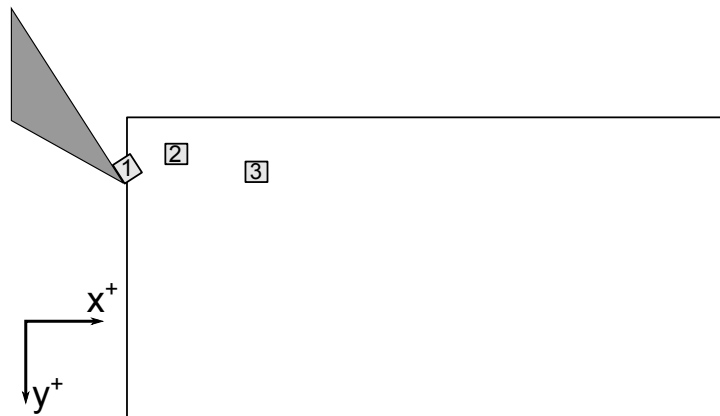


Figure 7. Locations of the averaged pressure nodes. The nodes move with the cutting tool

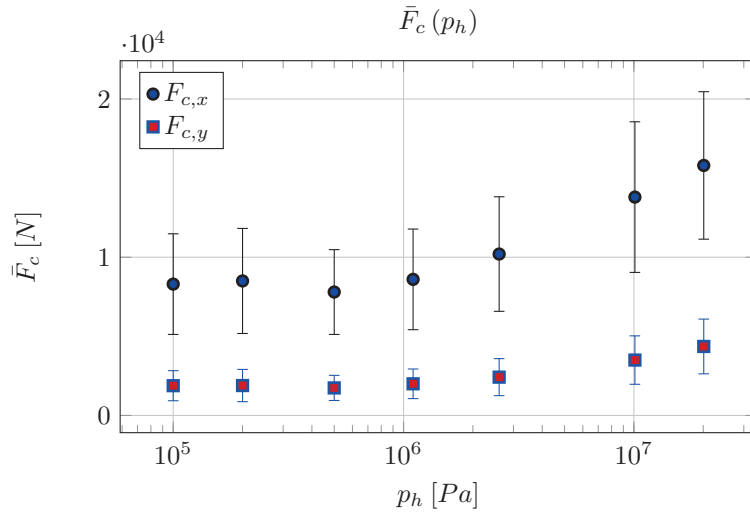


Figure 8. Cutting force vs hydrostatic pressure

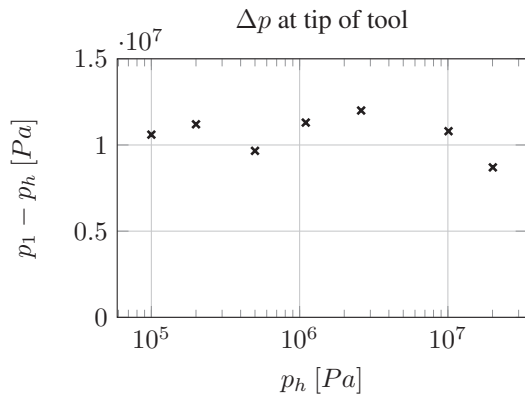


Figure 9. Averaged pressure difference in node 1 vs hydrostatic pressure, based on operating conditions as in table 1

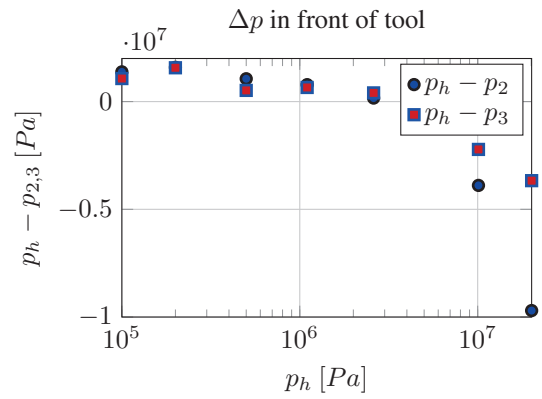


Figure 10. Averaged pressure difference in nodes 2 and 3 vs hydrostatic pressure, based on operating conditions as in table 1

Different types of behavior are noted, for shallow water depths the cutting process is dominated by tensile failures (see figure 11), for deep sea applications, the rock cutting process is dominated by shear failures (see figure 12).

5 DISCUSSION

A clear distinction is observed between low and high hydrostatic pressures. At low hydrostatic pressures, the cutting process is dominated by the occurrence of large chips. Those chips occur when the cutting process is dominated by tensile failures. At high hydrostatic pressures, the cutting process is dominated by shear failures. Chips still seem to occur in hyperbaric conditions, but these are significantly smaller, as can be seen in figures 11 and 12. The transition between the two regimes is at a water depth of 300 m, based on the operating conditions as in table 1.

Also notice that the vertical cutting force is significantly lower than the horizontal force, which does not correspond with experience from experiments. Such an effect is also noted in the DEM-simulations of dry rock cutting by Rojek et al. (2011). They noted that the vertical cutting force in 2D is strongly underestimated, while in 3D simulations this force is in the same range as in practice. Rojek et al. (2011) argue that this difference is caused by the lack of geometric information in 2D simulations, which seems valid considering that the 2D simulations are an approximation of plane strain.

At several points relative to the tool, the average pore pressures have been measured. The averaged pore pressure at the tip of the chisel (P1) shows no dependence on the hydrostatic pressure. This corresponds with the effective stress theory, initially the pore and hydrostatic pressures are in equilibrium and in the crushed zone, the deformation is always dominated by compression, leading to an increased pore pressure.

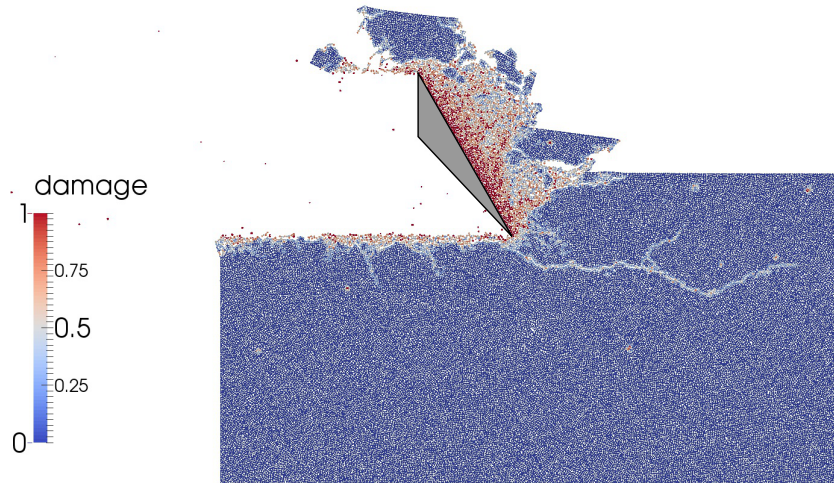


Figure 11. Damage during cutting at 0 m water depth. Damage is defined as $D = 1 - \frac{\# \text{ bonds}}{\# \text{ initial bonds}}$

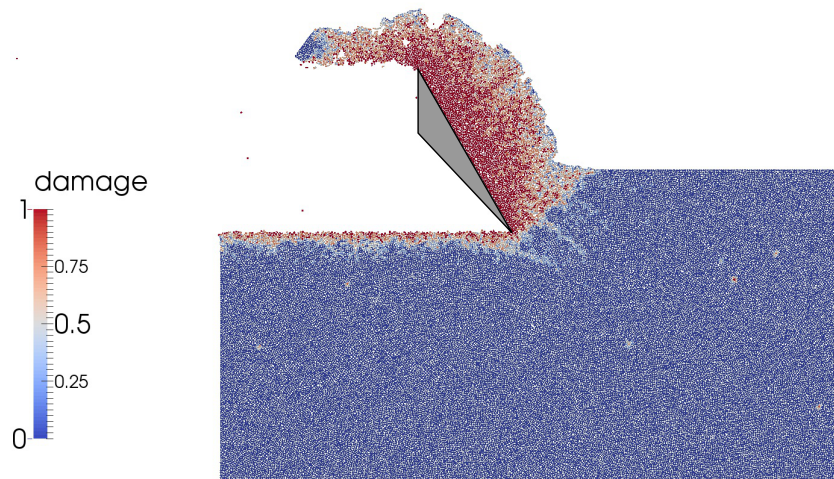


Figure 12. Damage during cutting at 2000 m water depth. Damage is defined as $D = 1 - \frac{\# \text{ bonds}}{\# \text{ initial bonds}}$

The averaged pore pressure measurements in front of the chisel (P3, P4) both show a transition from a pressure increase to a pressure drop (see figure 10). This can be explained as that the rock deformation is dominated by compression in shallow water depths and that it is dominated by dilation at large water depths. The fact that a positive averaged pressure difference is noted in shallow waters is caused by the brittle behavior of the cutting process. Before a chip can occur, the tool first needs to build up pressure to reach a stress condition where the rock starts to fail by the occurrence of macro-cracks. However, the exact location of these cracks always differs and those are often outside the pressure averaging areas. In that sense, the average pressure measured at P4 and P4 is often that of the pore pressure in an 'intact' chip. At large water depths, the rock failure is dominated by shear failures, resulting in dilation. As a result, the pressure drops in the dilative zone and the fluid has to flow towards it. In these water depths, the rock cutting process seems similar compared with the cutting of sand (which is also noted by Miedema and Zijlsling (2012)).

6 CONCLUSION

The DEM has been often used to simulate rock cutting processes of dry rock. An extension of DEM with SP to model the pore pressure effects gives promising results concerning the cutting of saturated rock. Two cutting regimes can be distinguished relative to the water depth, the tensile failure dominated regime for shallow water depths and the shear failure dominated regime for large water depths.

The results of the method correspond with observations in experiments and literature, more quantitative validation will be needed. This will be done in future work by comparing the simulations with cone indentation tests, rock cutting tests and (oil/gas) drilling tests.

ACKNOWLEDGEMENTS

This research is part of the PhD-project of EXHADERO (Excavation of Hard Deposits and Rock), which is performed with support of Delft University of Technology, Agentschap NL, Royal Dutch Shell, Royal Boskalis Westminster, Van Oord Dredging and Marine Contractors and Royal IHC. The authors are grateful for their support.

References

- Brace W. and Martin III R.** (1968). A test of the law of effective stress for crystalline rocks of low porosity. *International Journal of Rock Mechanics and Mining Sciences* 5, 415–426.
- Chen J.K., Beraun J.E. and Carney T.C.** (1999). A corrective smoothed particle method for boundary value problems in heat conduction. *International Journal for Numerical Methods in Engineering* 252(June 1998), 231–252.
- Cleary P.W. and Monaghan J.J.** (1999, January). Conduction modelling using Smoothed Particle Hydrodynamics. *Journal of Computational Physics* 148(1), 227–264.
- Coussy P.O.** (2004). *Poromechanics*. West Sussex: John Wiley & Sons Ltd.
- Detournay E. and Atkinson C.** (2000, October). Influence of pore pressure on the drilling response in low-permeability shear-dilatant rocks. *International Journal of Rock Mechanics and Mining Sciences* 37(7), 1091–1101.
- Evans I.** (1965, March). The force required to cut coal with blunt wedges. *International Journal of Rock Mechanics and Mining Sciences & Geomechanics Abstracts* 2(1), 1–12.
- Huang H.** (1999). *Discrete element modeling of tool-rock interaction*. Doctoral, University of Minnesota.
- Huang H., Lecampion B. and Detournay E.** (2013). Discrete element modeling of tool-rock interaction I : rock cutting. *International Journal for Numerical and Analytical Methods in Geomechanics* 37(13), 1913–1929.
- Lei S. and Kaitkay P.** (2003). Distinct Element Modeling of Rock Cutting under Hydrostatic Pressure. *Key Engineering Materials* 250, 110–117.
- Lucy L.** (1977). A numerical approach to the testing of the fission hypothesis. *Astronomical Journal*, 1013–1024.
- Mendoza Rizo J.** (2013). *Considerations for discrete element modeling of rock cutting*. Doctoral, University of Pittsburgh.
- Miedema S.** (2014). *The delft sand, clay & rock cutting model*. Amsterdam, the Netherlands: IOS Press.
- Miedema S.A. and Zijsling D.** (2012). Hyperbaric rock cutting. In *OMAE 2012*, Rio de Janeiro, Brasil.
- Muhammad N., Rogers B.D. and Li L.** (2013, March). Understanding the behaviour of pulsed laser dry and wet micromachining processes by multi-phase smoothed particle hydrodynamics (SPH) modelling. *Journal of Physics D: Applied Physics* 46(9), 095101.
- Nishimatsu Y.** (1972). The mechanics of rock cutting. *International Journal of Rock Mechanics and Mining Sciences* 9, 261–270.
- Potyondy D. and Cundall P.** (2004, December). A bonded-particle model for rock. *International Journal of Rock Mechanics and Mining Sciences* 41(8), 1329–1364.
- Rojek J., Oñate E., Labra C. and Kargl H.** (2011, September). Discrete element simulation of rock cutting. *International Journal of Rock Mechanics and Mining Sciences* 48(6), 996–1010.
- Su O. and Akcin N.A.** (2011). Numerical simulation of rock cutting using the discrete element method. *International Journal of Rock Mechanics and Mining Sciences* 48(3), 434–442.
- Swan G., Cook J., Bruce S. and Meehan R.** (1989, March). Strain rate effects in Kimmeridge bay shale. *International Journal of Rock Mechanics and Mining Sciences & Geomechanics Abstracts* 26(2), 135–149.
- Terzaghi K.** (1943). *Theoretical Soil Mechanics*. John Wiley and Sons.
- van Kesteren W.G.M.** (1995). Numerical simulations of crack bifurcation in the chip forming cutting process in rock. *Fracture of Brittle Disordered Materials: concrete, Rock and Ceramics* 26(1-2), 21–25.

Wendland H. (1995). Piecewise polynomial positive definite and compactly supported radial functions of minimal degree. *Advances in Computational Mathematics* 4, 389–396.

Zijsling D. (1987). Single cutter testing - A key for PDC bit development. In *Offshore Europe 87*, Aberdeen, UK, pp. SPE16529/1.